



Trans. Nonferrous Met. Soc. China 33(2023) 3725-3738

Transactions of Nonferrous Metals Society of China

www.tnmsc.cn



Influence of pore structures on deformation behavior and mechanical properties of porous tantalum scaffolds fabricated by electron beam powder bed fusion

Yu GUO^{1,2,3}, Chao CHEN¹, Yan-ming PAN², Qiang-bing WANG^{2,3}, Chen WU³, Ke-chao ZHOU¹

- 1. State Key Laboratory of Powder Metallurgy, Central South University, Changsha 410083, China; 2. Guangzhou Sailong Additive Manufacturing Co., Ltd., Guangzhou 510700, China;
- 3. State Key Laboratory of Porous Metal Materials, Northwest Institute for Nonferrous Metal Research, Xi'an 710016, China

Received 14 July 2022; accepted 22 March 2023

Abstract: Porous tantalum scaffolds with the dodecahedron, G7, and cubic structures were fabricated by electron beam powder bed fusion (EB-PBF). The influence of pore structures on the deformation behavior and mechanical properties of porous tantalum scaffolds was investigated by compressive testing, tensile testing, three-point bending testing, and finite element analysis (FEA). In the compressive test, the deformation of G7 and cubic scaffolds was dominated by buckling. The dodecahedron scaffold was deformed mainly by bending, leading to its lower compressive strength. On the other hand, the dodecahedron scaffold had superior tensile and bending properties. The uniform maximum stress distributions of the dodecahedron scaffold in the tensile and bending tests contributed to the homogeneous structural deformation, which delayed the fracture of struts; whereas, the maximum stresses of G7 and cubic scaffolds were concentrated in the transverse struts, resulting in the fracture of transverse struts in the early deformation stage. Therefore, pore structures should be properly selected for EB-PBF manufactured porous tantalum scaffolds based on the requirements for mechanical properties.

Key words: additive manufacturing; porous tantalum scaffold; electron beam powder bed fusion; pore structure; deformation behavior; mechanical properties

1 Introduction

Replacing damaged bone tissue with metal implants is an effective approach for orthopedic diseases. Porous tantalum scaffold has been clinically used in bone tissue repair due to its excellent corrosion resistance, high friction coefficient, suitable mechanical properties, outstanding osteoconductivity, and osteoinductivity [1]. With the popularization of precision medicine, clinical requirements for the precision and personalization of bone repair implants have surged in recent years. However, the porous

tantalum implants prepared by traditional methods can hardly meet these requirements anymore [2]. Additive manufacturing (AM) is a new processing technology developed in the past decades, which has been demonstrated to be capable of fabricating porous implants made of titanium alloy [3,4], stainless steel [5], and cobalt-based alloy [6].

Moreover, the external size and internal pore structure of the porous implants can be precisely regulated by controlling the processing parameters of AM [7]. The AM technologies for fabricating porous implants mainly include laser powder bed fusion (L-PBF) and electron beam powder bed fusion (EB-PBF) [8]. Compared with L-PBF, EB-PBF

fabricates implants in a vacuum environment, giving the parts a high degree of cleanliness. In addition, EB-PBF has the advantages of high-temperature preheating (up to 1100 °C), post-deposition thermal compensation, and high-energy electron beam melting, which can effectively alleviate the local thermal stress in the forming process and avoid the formation of pores and cracks in the produced components [9]. It is more suitable for manufacturing refractory and medical metal materials, such as tantalum.

Based on the studies of other porous metal scaffolds manufactured by EB-PBF, porosity, and pore structure are the key factors affecting the mechanical properties of scaffolds [10]. With the increase of porosity, the mechanical properties of porous metal scaffolds decrease gradually [11]. Besides porosity, the pore structure is another major factor affecting the mechanical properties of porous metal scaffolds [12]. Compared to titanium alloy and stainless steel, tantalum has lower strength but better ductility, which makes the deformation behavior of porous tantalum scaffolds different from other materials [13]. Therefore, it is necessary systematically investigate the influence of pore structure on the deformation behavior and mechanical properties of porous tantalum scaffolds. In addition, the real physiological environment is extremely complex and unpredictable, and implants need to bear the loads from multiple directions with different motion states of the human body [1], and the comprehensive mechanical properties including compressive tensile property, and bending properties should also be concerned. However, few researches have reported EB-PBF manufactured porous tantalum scaffolds so far. The studies on mechanical properties of porous scaffolds mainly focused on the compressive strength of specific pore structure. The effects of pore structures on the compressive, tensile and bending properties remain unclear.

In this work, the porous tantalum scaffolds with different pore structures were produced by EB-PBF. Compressive, tensile, and three-point bending tests were conducted on the EB-PBF fabricated tantalum scaffolds. The influence of pore structures on the deformation behavior and mechanical properties of tantalum scaffolds was revealed, which would provide innovative insights and inspiration for the design, preparation, and

clinical application of high-performance porous tantalum implants.

2 Experimental

2.1 Raw powder and EB-PBF process

The spherical tantalum powder prepared by the plasma rotating electrode process (PREP) was supplied by Xi'an Sailong Metal Materials Co., Ltd. The oxygen content of tantalum powder was about 0.046 wt.%. The apparent density, tap density, flowability (relative to 50 g sample), and particle size distribution of raw powder are listed in Table 1. A Sailong Y150 EB-PBF system operated at the voltage of 60 kV was used to manufacture the porous tantalum scaffolds with different pore structures. Before the EB-PBF process, the preparation, involving powder loading, thermocouple calibration, substrate leveling, and powder quantity debugging, was completed. The beam current and scanning speed were 17 mA and 0.4 m/s, respectively. The contour lines and indent contour lines of section information in each layer were scanned. Each contour line was composed of points with a space of 100 µm. The layer thickness was 50 µm, and the vacuum pressure was lower than 10^{-2} Pa. The substrate with dimensions of 170 mm × 170 mm × 10 mm was preheated to over 700 °C before the EB-PBF process. The layer preheating was performed before and after powder laying. The electron beam current, scanning speed, and the preheating time for layer preheating were 35 mA, 13 m/s, and 15 s, respectively. After the EB-PBF process, the unfused powder in the samples was removed by compressed air flushing and ultrasonic cleaning.

As shown in Fig. 1, the dodecahedron with strut angle of 35.3° , G7, and cubic were selected as the unit cells of tantalum scaffolds. The dimensions of the three unit cells were $2.5 \text{ mm} \times 2.5 \text{ mm} \times 2.5 \text{ mm}$, and the designed porosities were 87.4%, 76.9%, and 71.8%, respectively.

Table 1 Apparent density, tap density, flowability, and particle size of tantalum powder

| Apparent density/ (g·cm ⁻³) | density/ | Flowability/ s | <i>D</i> ₁₀ / μm | D ₅₀ / μm | D ₉₀ / μm |
|---|----------|-------------------|-----------------------------|-------------------------|-------------------------|
| 10.24 | 11.3 | 8.6 | 74.5 | 116 | 182 |

 D_{10} , D_{50} , and D_{90} are particle diameters corresponding to cumulative volume fractions less than 10%, 50%, and 90%, respectively

2.2 Characterization of surface morphology and mechanical properties

The porosity (ρ) of the porous tantalum scaffold was calculated by

$$\rho = [1 - (m_1/m_2)] \times 100\% \tag{1}$$

where m_1 denotes the actual mass of the porous tantalum scaffold, m_2 denotes the theoretical mass of dense tantalum with the same volume, and the theoretical density of pure tantalum (16.68 g/cm³) was used.

The surface morphology of the tantalum scaffold was characterized by scanning electron microscopy (SEM, JSM 6460, Japan). The compressive, tensile, and bending properties were tested on an Instron 3369 machine at room temperature. A digital camera recorded the response of the scaffolds. The compressive testing was conducted according to the ISO 13314:2011 standard, except for the dimension of the cubic scaffold. The deformation rate was 1 mm/min. The compressive yield strength was the compressive 0.2% offset stress from the compressive stressstrain curve, and the compressive plateau strength was defined as the average stress at the strain between 20% and 30%. Tensile and three-point bending tests were performed according to the ISO 6892-1:2009 and YS/T 1131-2016 (Chinese Non-ferrous Metal Industry Standard), respectively, with a speed of 2 mm/min. The tensile yield strength and the bending yield strength were determined identically to the compressive yield strength. Figure 2 shows the sample schematic and dimensions of tantalum scaffolds for compressive, tensile, and three-point bending tests. Three samples were used for each type of test to ensure data reproduction.

ANSYS 2022R1 software was used to simulate the stress distributions of porous tantalum scaffolds with different pore structures during deformation. The multilinear plastic hardening

model was conducted. The modulus and Poisson ratio of tantalum were taken as 186 GPa and 0.35, respectively, accordingly. The compressive yield strength and tensile yield strength were set to be 285 and 331 MPa, respectively [14].

3 Results

3.1 Surface morphology and pore structure characteristics

Figure 3 shows the surface morphologies of porous tantalum scaffolds with different unit cells. It can be observed that the geometrical structures of the EB-PBF fabricated tantalum scaffolds are consistent with the designed models. Three types of scaffolds exhibit good melting quality; there are no production defects, such as broken struts or pores on the surface of the struts. However, partially fused particles are observed inside the G7 and cubic scaffolds. Since G7 and cubic scaffolds have larger designed strut diameters than the dodecahedron scaffolds, insufficient energy input causes the partial melting of tantalum powder attached to the struts. The detailed pore structure characteristics of EB-PBF fabricated tantalum scaffolds are listed in Table 2. The average pore sizes of the dodecahedron, G7, and cubic tantalum scaffolds are 326, 895, and 1220 µm, respectively. The statistical strut diameters are 531, 775, and 1320 µm, respectively.

3.2 Compressive property

The compressive stress-strain curves of the three tantalum scaffolds are shown in Fig. 4. As shown in Fig. 4(a), due to the excellent ductility of tantalum, no maximum stress or maximum strain is observed in the compressive curves, which is similar to other studies on the compressive performance of porous tantalum scaffold [15,16]. The compressive curves of three tantalum scaffolds can be divided into three stages, that is, elastic,

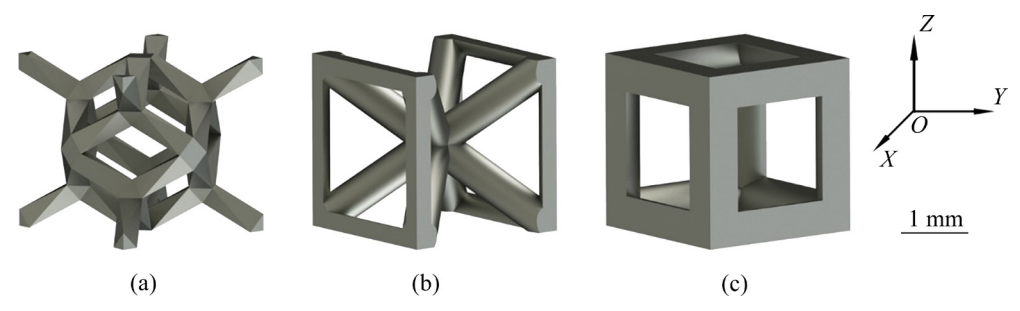


Fig. 1 3D visual representations of applied unit cells: (a) Dodecahedron; (b) G7; (c) Cubic

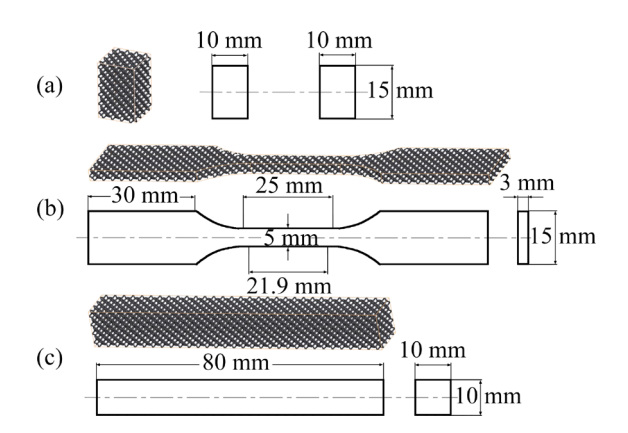


Fig. 2 Sample schematic and dimensions for compressive (a), tensile (b), and three-point bending (c) tests

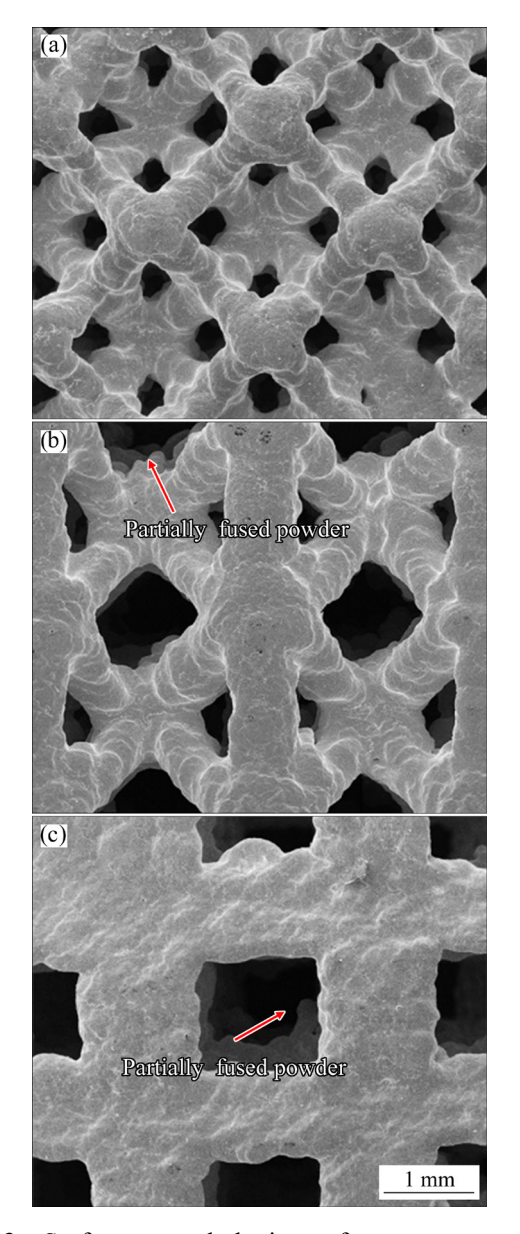


Fig. 3 Surface morphologies of porous tantalum scaffolds with different unit cells: (a) Dodecahedron; (b) G7; (c) Cubic

 Table 2
 Pore structure characteristics of EB-PBF manufactured tantalum scaffolds

| Structure | Strut size/µm | Pore size/ μm | Porosity/% |
|--------------|---------------|--------------------|-----------------|
| Dodecahedron | 531±26 | 326±35 | 70.9±0.17 |
| G 7 | 775±40 | 895±42 | 70.2 ± 0.32 |
| Cubic | 1320±50 | 1220±52 | 70.33±0.21 |

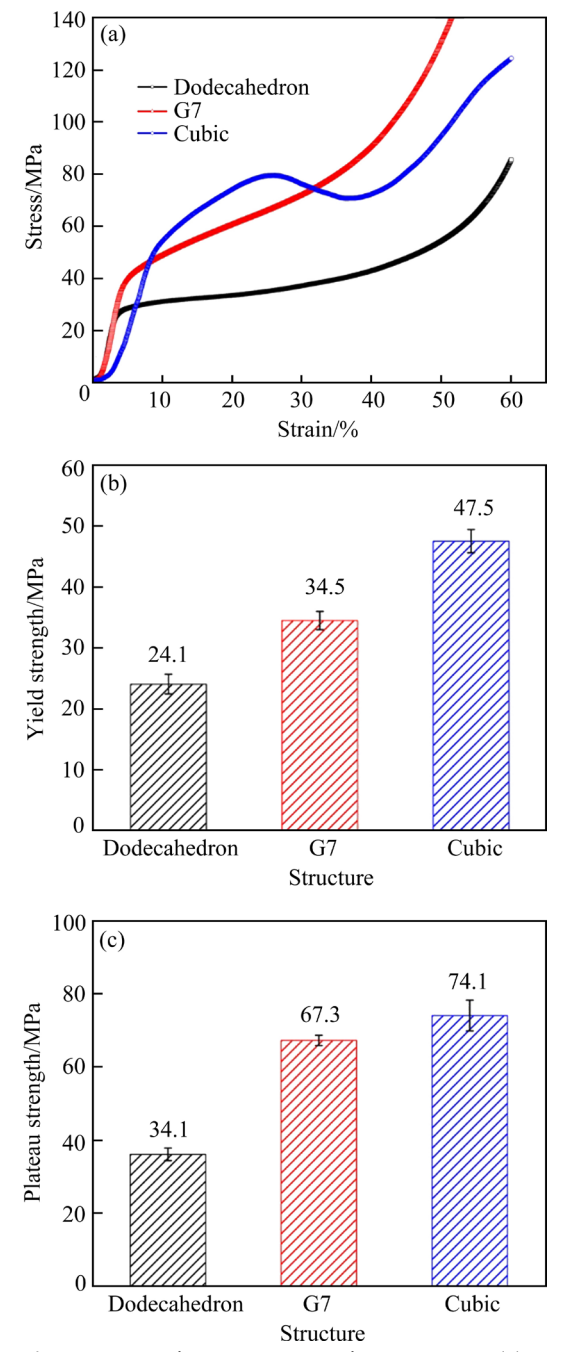


Fig. 4 Compressive stress–strain curves (a) and compressive properties (b, c) of porous tantalum scaffolds with different structures

platform, and compaction. Different from the smooth platform areas of dodecahedron and G7 tantalum scaffolds, the curve of the cubic tantalum scaffold suddenly drops after entering the platform stage, which is caused by the collapse of the unit cells. The porous tantalum scaffold with the unit cell of dodecahedron exhibits the lowest compressive yield strength of 24.1 MPa and compressive plateau strength of 36.1 MPa, while the cubic scaffold has the highest compressive properties, the compressive yield strength and compressive plateau strength are 47.5 and 74.1 MPa, respectively. The compressive strength of the G7 scaffold is between that of the dodecahedron and cubic scaffolds. Compared with the dodecahedron and G7 porous tantalum scaffolds, the deviation in the compressive strength of the cubic scaffold is relatively large.

Figure 5 shows the geometrical structure evolution of three tantalum scaffolds during the compressive testing. Under vertical loading, the

struts of dodecahedron tantalum scaffold are mainly deformed by bending deformation, and the strut angle decreases gradually as the compressive strain increases. The cubic scaffold exhibits progressive collapse behavior due to vertical struts, including buckling and bending deformation. The buckling deformation first takes place on the vertical struts. When the compressive stress exceeds the yield strength, the vertical struts are subjected to bending deformation until some unit cells collapse. The stress-strain curve of the cubic scaffold shows a sudden drop trend, which is consistent with the phenomenon reported by GAO et al [17]. Due to the existence of inclined struts, the collapse of the pore structure of G7 is not obvious during the compressive test. When the vertical struts fail, the compressive stress is transferred to the inclined struts to cause them to bend.

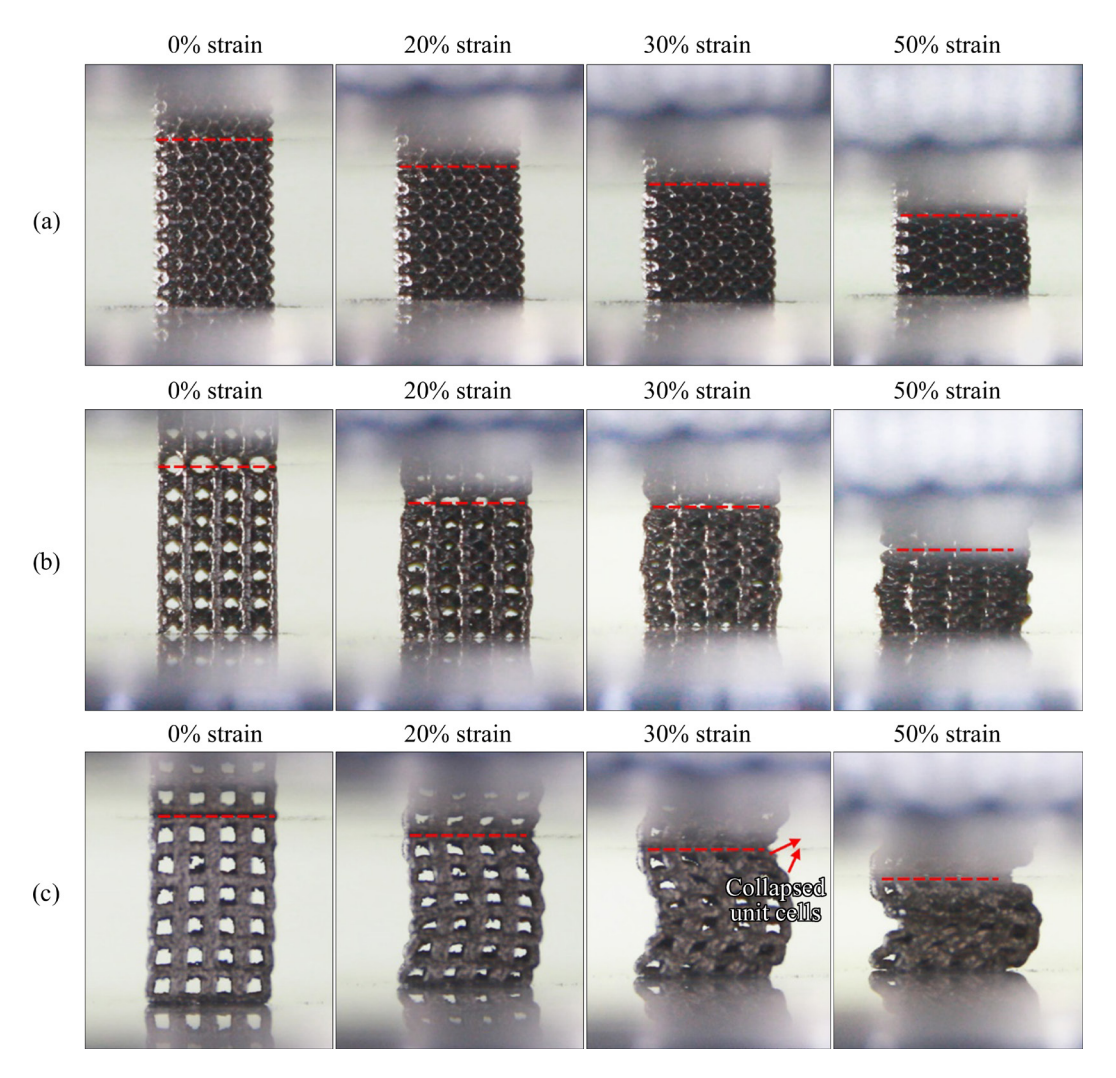


Fig. 5 Geometrical morphologies of tantalum scaffolds with different structures at strains of 0%, 20%, 30%, and 50%: (a) Dodecahedron; (b) G7; (c) Cubic

3.3 Tensile property

Figure 6 exhibits the tensile stress-strain curves and tensile properties of tantalum scaffolds with different porous structures. As shown in Fig. 6(a), the tensile stress-strain curves of three scaffolds are divided into the elastic, plastic, and fracture stages. The dodecahedron tantalum scaffold has a long plastic stage, and its tensile stress-strain curve is smooth. In contrast, the plastic stages of G7 and cubic scaffolds are shorter and fluctuate continuously due to the fracture of struts. Pore structures strongly influence the tensile properties of tantalum scaffolds. The tensile yield strengths of dodecahedron, G7, and cubic porous tantalum scaffolds are 27.6, 26.2, and 18.4 MPa, respectively. Large deviations are observed in the measured tensile yield strength of G7 and cubic scaffolds. The corresponding tensile strains of the corresponding three porous tantalum scaffolds are 19.3%, 8.0%, and 5.6%, respectively.

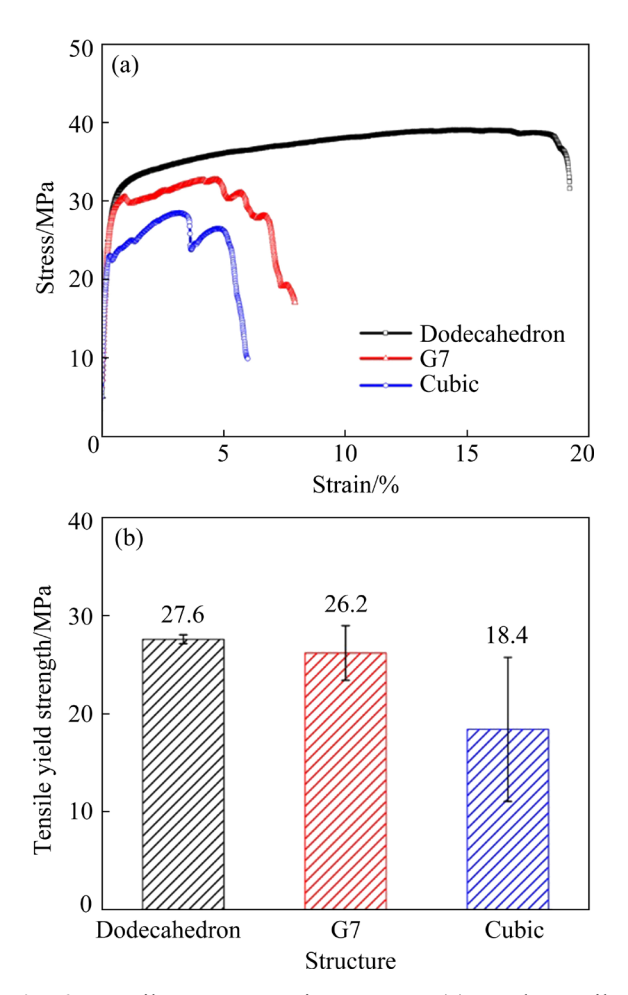


Fig. 6 Tensile stress-strain curves (a) and tensile properties (b) of porous tantalum scaffolds with different structures

Figure 7 displays geometrical morphologies of tantalum scaffolds during tensile testing. As shown in Fig. 7(a), the fracture point initially appears near the strut intersections and then propagates along the fracture surface until the strut breaks. With increasing the strain, multiple struts break until the sample finally fails. The transverse struts are first destroyed at a relatively low tensile strain for the G7 scaffold (Fig. 7(b)). Subsequently, the inclined struts of the G7 scaffold gradually break like the dodecahedron one. Under the tensile stress, the major fracture mode of cubic tantalum scaffold is the successive break of transverse struts. In addition, a slight torsional deformation is observed in the tensile deformation of the cubic tantalum scaffold.

Figure 8 displays the fracture surfaces of the struts of three tantalum scaffolds. The fracture surface exhibits a mixture of cleavage facets and unfused powder, showing an obvious brittle fracture characteristic. This phenomenon differs from the ductile fracture characteristic of EB-PBF fabricated dense tantalum, presenting many dimples on the fracture surface [18]. The main reason is that the diameter of the strut is small. Once the crack nucleates, there are inadequate grains inside the strut to hinder the propagation of the crack. Hence, the strut breaks quickly without plastic deformation.

3.4 Bending property

The bending stress-strain curves and bending properties of porous tantalum scaffolds with different porous structures are shown in Fig. 9. It can be found that the curves of G7 and cubic scaffolds drop immediately after reaching the highest stress, while the dodecahedron has no downward trend. The bending yield strengths of the dodecahedron and G7 scaffolds are close, 48.8 and 47.8 MPa, respectively, and the latter has a larger deviation. The cubic tantalum scaffold has the lowest bending yield strength of 31 MPa and the largest deviation.

Figure 10 displays the geometrical structure evolution of three tantalum scaffolds during bending deformation. During the bending process, the dodecahedron tantalum scaffold has no obvious fracture of the strut, which is similar to the results observed by TANG et al [19]. In contrast, the struts

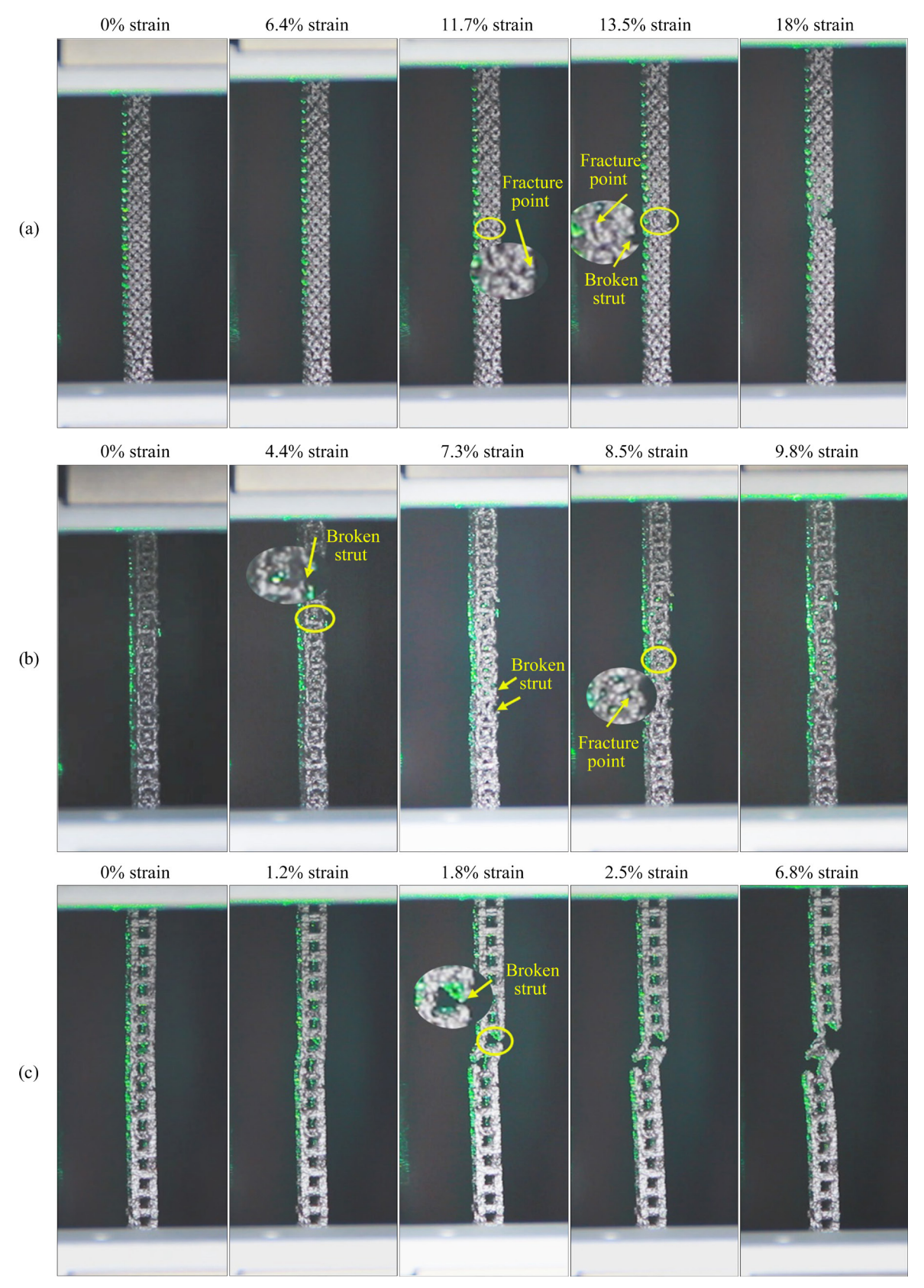


Fig. 7 Geometrical morphologies of tantalum scaffolds at different tensile strains: (a) Dodecahedron; (b) G7; (c) Cubic

of G7 and cubic scaffolds break during bending deformation. For the G7 scaffold, the fracture initially occurs in the bottom transverse strut, and

then the inclined struts in the same layer break. After one layer is destroyed, the neighboring layer is broken similarly until the whole structure is

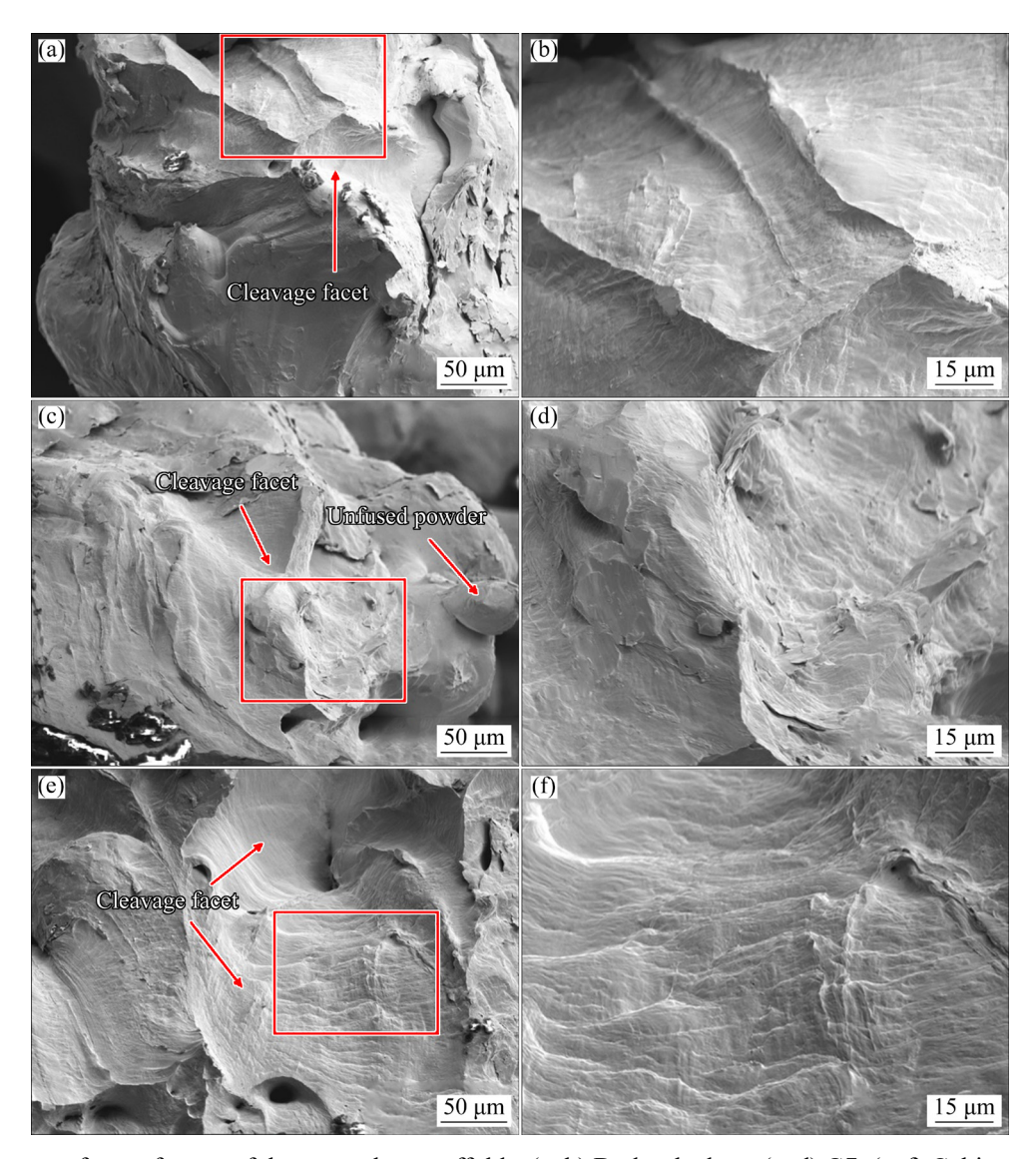


Fig. 8 Fracture surfaces of struts of three tantalum scaffolds: (a, b) Dodecahedron; (c, d) G7; (e, f) Cubic

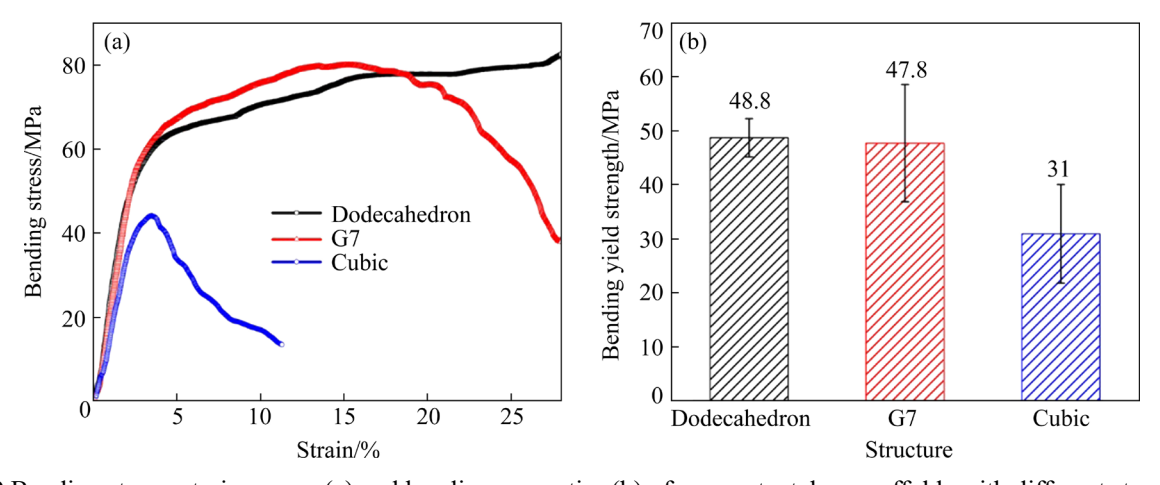


Fig. 9 Bending stress-strain curves (a) and bending properties (b) of porous tantalum scaffolds with different structures

completely damaged. The transverse struts gradually break from bottom to top in the bending process for the cubic scaffold. The surface

morphologies of tantalum scaffolds after bending are shown in Fig. 11. A few cracks are found on the bottom struts of the dodecahedron tantalum scaffold.

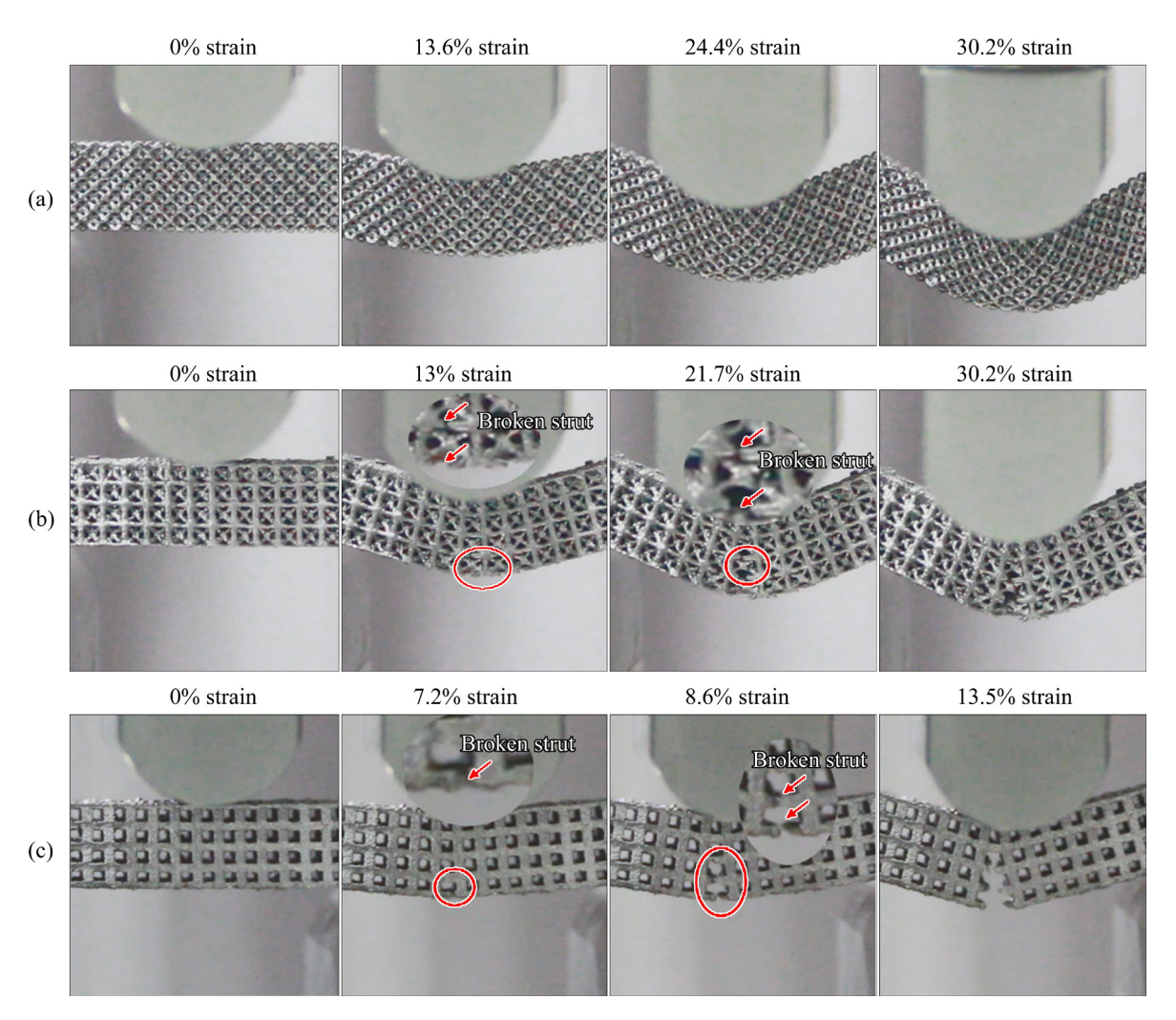


Fig. 10 Geometrical structure evolution of tantalum scaffolds with different structures during bending deformation: (a) Dodecahedron; (b) G7; (c) Cubic

As shown in Fig. 11(d), similar to the tensile fracture surface, the fracture surface of the cubic struts also presents a brittle fracture characteristic.

4 Discussion

4.1 Effect of pore structure on mechanical properties of tantalum scaffolds

Due to the high energy input during the EB-PBF process, the strut diameter of manufactured scaffold is oversized because of over-sintered powder at the edge of the processing path. For the scaffolds with different structures, the discrepancies between designed and fabricated porosities are attributed to the number of struts in each unit cell. As shown in Fig. 1, the number of struts in each unit cell decreases in the order of dodecahedron, G7, and cubic scaffolds. To obtain the identical

fabricated porosity, the designed porosity of structures decreases in the order of dodecahedron, G7, and cubic scaffolds. According to the Gibson-Ashby model, as the fabricated porosity decreases, the strength of porous tantalum scaffolds increases [20]. It is worth noting that the mechanical properties of the EB-PBF-produced tantalum scaffolds are lower than those with the same porosity in the ideal state. The over-sintered powder on the strut leads to the stress concentration, which accelerates the failure of the scaffold. In addition, although the fabricated porosity of the dodecahedron scaffold is similar to that of G7 and cubic scaffolds, the design porosity of the dodecahedron scaffold is the highest, which means that more over-sintered powder is attached to the struts. It enlarges the difference between the actual and designed states.

Previous studies proved that different pore structures result in various stress distributions, which leads to diverse deformation behavior [21,22]. Figure 12 displays the stress distributions of tantalum scaffolds under the identical compressive strain of 5%. For the dodecahedron tantalum scaffold, the maximum stress is distributed uniformly at all inclined struts intersections. In contrast, the maximum stresses of G7 and cubic scaffolds are mainly concentrated on the vertical struts. When the specimen is subjected to the axial

force, the intersections of the dodecahedron scaffold gradually approach, and the strut angle decreases. Inclined struts are deformed by bending at the initial stage of compressive deformation until the scaffolds are compacted (Fig. 5(a)). In comparison, the vertical struts of G7 and cubic scaffolds are deformed by buckling, manifested as instability of struts in Fig. 5(b) and Fig. 5(c). In the study of EB-PBF fabricated porous Ti₆Al₄V scaffolds, it was found that scaffolds dominated by buckling deformation show the relatively high

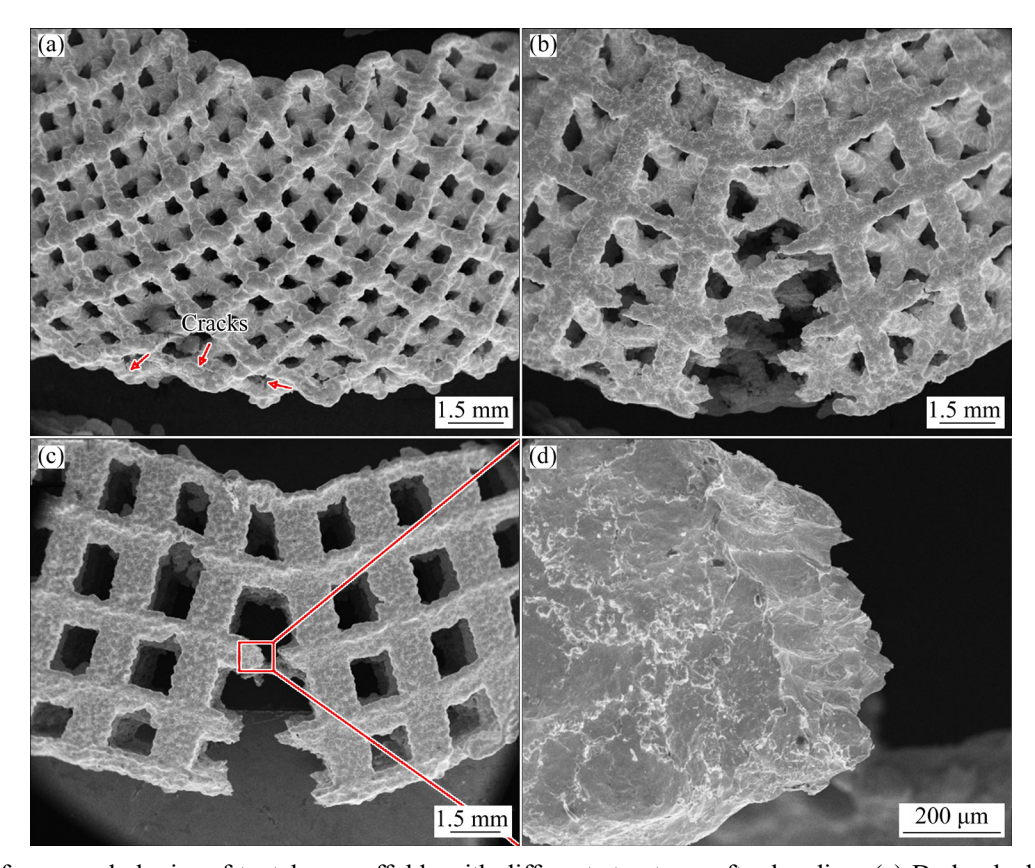


Fig. 11 Surface morphologies of tantalum scaffolds with different structures after bending: (a) Dodecahedron; (b) G7; (c, d) Cubic

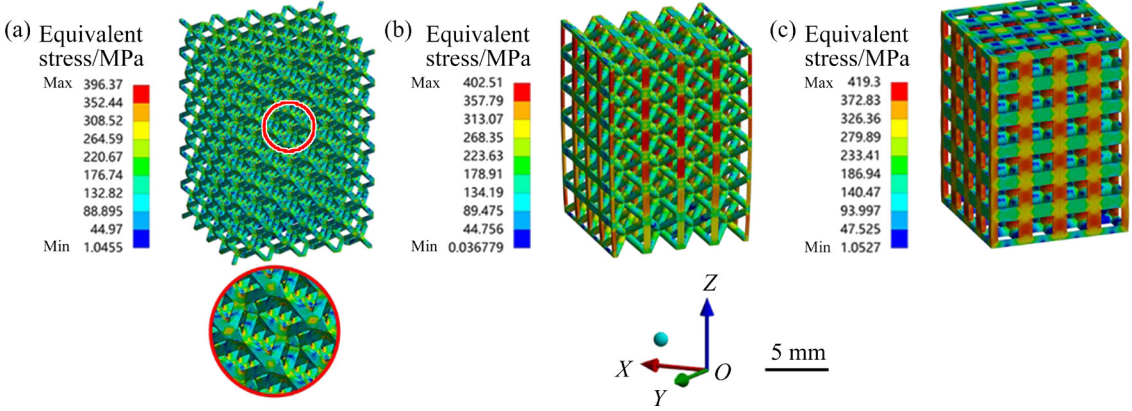


Fig. 12 Stress distributions of tantalum scaffolds at identical compressive strain of 5%: (a) Dodecahedron; (b) G7; (c) Cubic

compressive properties [10]. Therefore, the G7 and cubic tantalum scaffolds have higher compressive properties than the dodecahedron one.

Figure 13 shows the stress distributions of tantalum scaffolds at the tensile strain of 5%. Similar to the compressive state, the maximum stress of the dodecahedron sample is uniformly distributed at the intersections of struts, and the maximum stresses of G7 and cubic samples are concentrated on the transverse struts. However, the tensile yield strength and tensile strain of three scaffolds decrease in the order of dodecahedron, G7, and cubic scaffolds. As shown in Fig. 7(a), the fracture point appears near the intersections of struts until the tensile strain exceeds 11%. In comparison, the transverse struts of the G7 and cubic scaffolds break when the strains are less than 5% and 2%, respectively. Under the tensile loading, the overall structure of the dodecahedron scaffold undergoes uniform deformation first. As the displacement increases constantly, the inclined struts can rotate slightly around the intersections, which can delay the fracture of the struts [23]. With further increasing the tensile strain of the dodecahedron scaffold, a progressive fracture

evolves as the crack propagation occurs. Unfortunately, because the procedure is extremely rapid, the digital camera does not record the whole process of strut fracture. In contrast, as the dominant bearing component, the transverse struts of G7 and cubic scaffolds experience larger plastic deformation than their other struts, resulting in a premature fracture in the early deformation stage. Therefore, during the tensile test, the transverse struts of G7 and cubic scaffolds are sensitive to the defects such as residual pores.

As shown in Fig. 14, during the bending deformation, for the upper surface contacting with the indenter, the scaffold is mainly subjected to compressive stress, including the downward extrusion of the indenter and the extrusion between the unit cells. Correspondingly, the lower surface of the scaffold is mainly subjected to tensile stress, which makes the struts of the lower surface easier to damage. Similar to the tensile test, the transverse struts on the lower surfaces of G7 and cubic scaffolds are the dominant bearing components for tensile stress, and the struts are prone to break at the defects, as shown in Fig. 10. Due to the uniform stress distribution, the dodecahedron scaffold can

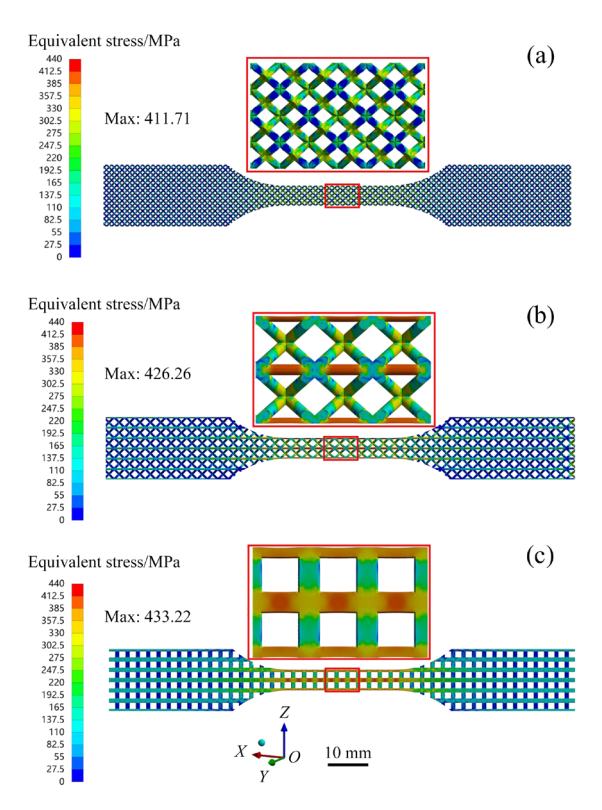


Fig. 13 Stress distributions of tantalum scaffolds at identical tensile strain of 5%: (a) Dodecahedron; (b) G7; (c) Cubic

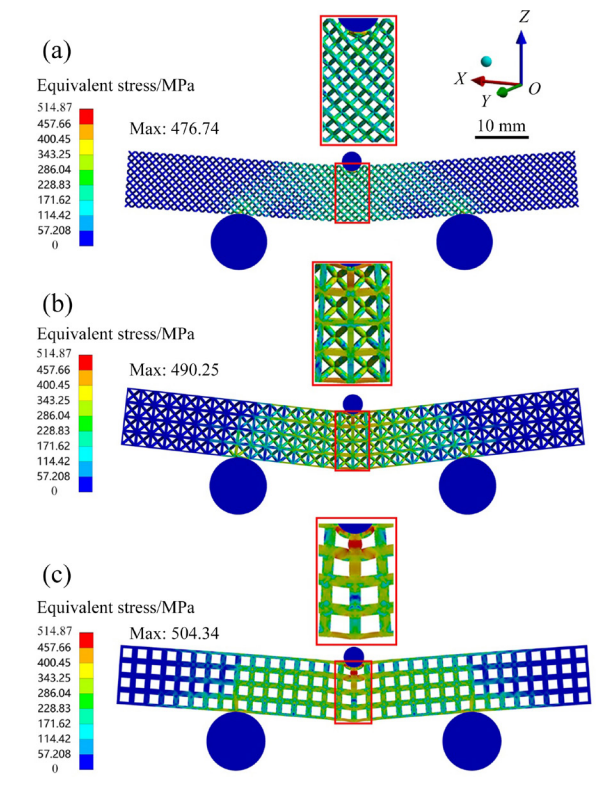


Fig. 14 Stress distributions of tantalum scaffolds during bending deformation: (a) Dodecahedron; (b) G7; (c) Cubic

delay the fracture of struts by structural deformation in the bending deformation process. Hence, the dodecahedron scaffold has higher strength and stability than G7 and cubic scaffolds.

The failure of a porous metal scaffold is always accompanied by structural damage and material damage [20]. Due to the excellent ductility of tantalum, the tantalum scaffold is gradually compacted without fracture of struts in the compressive test. The deformation mode is an important factor affecting the mechanical properties of scaffolds. In the process of tensile and bending, the maximum stresses of cubic and G7 scaffolds are mainly distributed on the transverse struts, and hence the transverse struts break directly at the defects in the early deformation stage. However, for the dodecahedron scaffold, the fracture of struts is delayed by structural deformation during the tensile and bending processes. Hence, the dodecahedron tantalum scaffold has lower compressive properties but superior tensile and bending properties.

As shown in Fig. 12, under the same compressive strain, the maximum stress of three tantalum scaffolds increases in the order of dodecahedron, G7, and cubic scaffolds, which is consistent with testing results. However, under the same tensile strain and bending strain, the maximum stress of simulation results decreases in the order of cubic, G7, and dodecahedron scaffolds, which differs from the testing results. In the finite element simulation, the tantalum strut is assumed to have a smooth surface, no defects inside, and no strut fracture during deformation. Indeed, the surface of EB-PBF-manufactured tantalum struts is rough and irregular, and defects such as pores are inevitably inside. In the compressive deformation, only structural damage occurs, consistent with the simulation. Hence, the simulation results in compressive deformation fit well with the testing results. In the process of tensile and bending, imperfections promote material damage, which differs from the simulation. Therefore, the tensile strength and bending strength of G7 and cubic scaffolds are significantly smaller than simulation results.

4.2 Comparison with human bones

Like other materials, the mechanical properties of porous tantalum implants used in clinical orthopedics should be compatible with human bone. If the mechanical strengths of porous tantalum implants are higher than those of the natural bones, the stress shielding phenomenon will occur during the service process, resulting in bone dissolution around the implant [24]. If the strength of implant is too low, it cannot effectively play a role in the repair and reconstruction of bone tissue. Table 3 compares the mechanical properties of tantalum scaffolds in this work and human bones. The compressive strength, tensile strength, and bending strength of EB-PBF manufactured tantalum scaffolds with different structures are also higher than those of human cancellous bone and lower than those of human cortical bone. Consequently, the sufficient mechanical properties of tantalum scaffolds in this study make them suitable for implant materials.

Table 3 Comparison of mechanical properties of tantalum scaffolds in this study with human bones

| Sample | Compressive strength/ MPa | | _ | Source |
|-----------------------------------|---------------------------------|---------|-----------|------------|
| Dodecahedron | 24.1 | 27.6 | 48.8 | This study |
| G7 | 34.5 | 26.2 | 47.8 | This study |
| Cubic | 47.5 | 18.4 | 31 | This study |
| Human cancellous bone-femur | 7.36 | 7.69-8 | 3.5 | [25-27] |
| Human cancellous bone-tibia | 5.33-10.6 | 2.54 | 1.86-4.26 | [25,28] |
| Human cortical bone-femur | 179-209 | 104-121 | 135-180 | [25,29] |
| Human cortical bone-tibia | 183-213 | 126-140 | 131 | [25,30] |

5 Conclusions

(1) In the compressive test, due to the excellent ductility of tantalum, no fracture of struts occurs until the scaffolds are compacted. The dodecahedron scaffold is deformed mainly by bending. The G7 and cubic scaffolds are dominated by buckling, leading to better compressive

properties than the dodecahedron scaffold.

- (2) The dodecahedron tantalum scaffold exhibits better tensile and bending properties than the G7 and cubic scaffolds in tensile and bending deformation. The maximum stress dodecahedron is uniformly distributed at the intersections of struts, resulting in homogeneous structural deformation before the fracture of the struts. However, as the dominant bearing component, the transverse struts of G7 and cubic scaffolds break in the very early deformation stage.
- (3) The mechanical properties of three types of tantalum scaffolds fall between those of the cortical and cancellous bones, indicating that they are suitable for implant materials.

Acknowledgments

The authors would like to acknowledge the financial supports from the Guangzhou Municipal Science and Technology Project, China (No. 202206010030), and the Key R&D Program of Guangdong Province, China (No. 2019B090904001).

References

- [1] GAO Hai-rui, YANG Jing-zhou, JIN Xia, QU Xin-hua, ZHANG Fa-qiang, ZHANG Da-chen, CHEN Hai-shen, WEI Hui-ling, ZHANG Shu-pei, JIA Wei-tao, YUE Bing, LI Xiao-peng. Porous tantalum scaffolds: Fabrication, structure, properties, and orthopedic applications [J]. Materials & Design, 2021, 210: 110095.
- [2] ZHOU Li-bo, YUAN Tie-chui, LI Rui-di, TANG Jian-zhong, WANG Guo-hua, GUO Kai-xuan. Selective laser melting of pure tantalum: Densification, microstructure and mechanical behaviors [J]. Materials Science and Engineering A, 2017, 707: 443–451.
- [3] HEINL P, MÜELLER L, KÖERNER C, SINGER R F, MÜELLER F A. Cellular Ti-6Al-4V structures with interconnected macro porosity for bone implants fabricated by selective electron beam melting [J]. Acta Biomaterialia, 2008, 4(5): 1536-1544.
- [4] COSTA M M, DANTAS T A, BARTOLOMEU F, ALVES N, SILVA F S, MIRANDA G, TOPTAN F. Corrosion behaviour of PEEK or β-TCP-impregnated Ti₆Al₄V SLM structures targeting biomedical applications [J]. Transactions of Nonferrous Metals Society of China, 2019, 29(12): 2523–2533.
- [5] NIENDORF T, BRENNE F, SCHAPER M. Lattice structures manufactured by SLM: On the effect of geometrical dimensions on microstructure evolution during processing [J]. Metallurgical and Materials Transactions B, 2014, 45(4): 1181–1185.
- [6] MURR L, LI Shu-jun, TIAN Yu-xing, AMATO K, MARTINEZ E, MEDINA F. Open-cellular Co-base and

- Ni-base superalloys fabricated by electron beam melting [J]. Materials, 2011, 4(4): 782-790.
- [7] JU Jiang, LI Jing-jing, JIANG Min, LI Meng-ya, YANG Li-xiang, WANG Kai-ming, YANG Chao, KANG Mao-dong, WANG Jun. Microstructure and electrochemical corrosion behavior of selective laser melted Ti-6Al-4V alloy in simulated artificial saliva [J]. Transactions of Nonferrous Metals Society of China, 2021, 31(1): 167-177.
- [8] LIU Yu-jing, LI Shu-jun, WANG Hao-liang, HOU Wen-tao, HAO Yu-lin, YANG Rui, SERCOMBE T B, ZHANG Lai-chang. Microstructure, defects and mechanical behavior of beta-type titanium porous structures manufactured by electron beam melting and selective laser melting [J]. Acta Materialia, 2016, 113: 56-67.
- [9] XIAO Bang, JIA Wen-peng, TANG Hui-ping, WANG Jian, ZHOU Lian. Microstructure and mechanical properties of a newly developed WTaRe refractory alloy by selective electron beam melting [J]. Additive Manufacturing, 2022, 54: 102738.
- [10] LI Shu-jun, XU Qin-si, WANG Zhen-bo, HOU Wen-tao, HAO Yu-lin, YANG Rui, MURR L E. Influence of cell shape on mechanical properties of Ti-6Al-4V meshes fabricated by electron beam melting method [J]. Acta Biomaterialia, 2014, 10(10): 4537-4547.
- [11] HORN T J, HARRYSSON O L A, MARCELLIN-LITTLE D J, WEST H A, LASCELLES B D X, AMAN R. Flexural properties of Ti₆Al₄V rhombic dodecahedron open cellular structures fabricated with electron beam melting [J]. Additive Manufacturing, 2014, 1/2/3/4: 2–11.
- [12] GUO Yu, CHEN Chao, TAN Li-ming, WANG Qiang-bing, PAN Yan-ming, ZHU Hao, ZHOU Ke-chao, WU Chen. The role of pore structures on the fatigue properties of additively manufactured porous tantalum scaffolds produced by electron beam powder bed fusion [J]. Journal of Materials Research and Technology, 2022, 19: 3461–3473.
- [13] YANG Jin-zhou, GAO Hai-rui, ZHANG Da-chen, JIN Xia, ZHANG Fa-qiang, ZHANG Shu-pei, CHEN Hai-shen, LI Xiao-peng. Static compressive behavior and material failure mechanism of trabecular tantalum scaffolds fabricated by laser powder bed fusion-based additive manufacturing [J]. International Journal of Bioprinting, 2022, 8(1): 438.
- [14] MARTIENSSEN W, WARLIMONT H. Handbook of condensed matter and materials data [M]. 2nd ed. Berlin: Springer, 2005.
- [15] YANG Jing-zhou, JIN Xia, GAO Hai-rui, ZHANG Da-chen, CHEN Hai-shen, ZHANG Shu-pei, LI Xiao-peng. Additive manufacturing of trabecular tantalum scaffolds by laser powder bed fusion: Mechanical property evaluation and porous structure characterization [J]. Materials Characterization, 2020, 170: 110694.
- [16] CHEN Wen-liang, YANG Jing-zhou, KONG Hui, HELOU M, ZHANG Da-chen, ZHAO Jin-hui, JIA Wei-tao, LIU Qian, HE Pei-dong, LI Xiao-peng. Fatigue behaviour and biocompatibility of additively manufactured bioactive tantalum graded lattice structures for load-bearing orthopaedic applications [J]. Materials Science and Engineering C, 2021, 130: 112461.
- [17] GAO Hai-rui, JIN Xia, YANG Jing-zhou, ZHANG Da-chen,

- ZHANG Shu-pei, ZHANG Fa-qiang, CHEN Hai-shen. Porous structure and compressive failure mechanism of additively manufactured cubic-lattice tantalum scaffolds [J]. Materials Today Advances, 2021, 12: 100183.
- [18] GUO Yu, CHEN Chao, WANG Qiang-bing, LIU Min. Effects of reuse on the properties of tantalum powders and tantalum parts additively manufactured by electron beam powder bed fusion [J]. Materials Research Express, 2021, 8(4): 046538.
- [19] TANG Hui-ping, YANG Kun, JIA Liang, HE Wei-wei, ZHANG Xue-zhe. Tantalum bone implants printed by selective electron beam manufacturing (SEBM) and their clinical applications [J]. JOM, 2020, 72(3): 1016–1021.
- [20] GIBSON L J, ASHBY M F. Cellular solids: Structure and properties [M]. 2nd ed. Cambridge: Cambridge University Press, 1997.
- [21] LIU Yu-jing, LI Shu-jun, ZHANG Lai-chang, HAO Yu-lin, SERCOMBE T B. Early plastic deformation behaviour and energy absorption in porous β-type biomedical titanium produced by selective laser melting [J]. Scripta Materialia, 2018, 153: 99–103.
- [22] XU Wei, YU Ai-hua, LU Xin, TAMADDON M, WANG Meng-di, ZHANG Jia-zhen, ZHANG Jian-liang, QU Xuan-hui, LIU Chao-zong, SU Bo. Design and performance evaluation of additively manufactured composite lattice structures of commercially pure Ti (CP-Ti) [J]. Bioactive Materials, 2021, 6(5): 1215–1222.
- [23] GENG Xiao-liang, LU Ya-hui, LIU Chao, LI Wei-nan, YUE Zhu-feng. Fracture characteristic analysis of cellular lattice

- structures under tensile load [J]. International Journal of Solids and Structures, 2019, 163: 170–177.
- [24] NIINOMI M, NAKAI M. Titanium-based biomaterials for preventing stress shielding between implant devices and bone [J]. International Journal of Biomaterials, 2011, 2011: 836587.
- [25] ZHANG X Z, LEARY M, TANG H P, SONG T T, QIAN M. Selective electron beam manufactured Ti-6Al-4V lattice structures for orthopedic implant applications: Current status and outstanding challenges [J]. Current Opinion in Solid State and Materials Science, 2018, 22(3): 75-99.
- [26] CARTER D R, SCHWAB G H, SPENGLER D M. Tensile fracture of cancellous bone [J]. Acta Orthopaedica Scandinavica, 1980, 51(5): 733–741.
- [27] SHERWOOD J K, RILEY S L, PALAZZOLO R, BROWN S C, MONKHOUSE D C, COATES M, GRIFFITH L G, LANDEEN L K, RATCLIFFE A. A three-dimensional osteochondral composite scaffold for articular cartilage repair [J]. Biomaterials, 2002, 23(24): 4739–4751.
- [28] RØHL L, LARSEN E, LINDE F, ODGAARD A, JØRGENSEN J. Tensile and compressive properties of cancellous bone [J]. Journal of Biomechanics, 1991, 24(12): 1143–1149.
- [29] ZIOUPOS P, CURREY J D. Changes in the stiffness, strength, and toughness of human cortical bone with age [J]. Bone, 1998, 22(1): 57-66.
- [30] BEAUPIED H, LESPESSAILLES E, BENHAMOU C L. Evaluation of macrostructural bone biomechanics [J]. Joint Bone Spine, 2007, 74(3): 233–239.

孔结构对电子束粉末床熔融多孔钽支架变形行为及 力学性能的影响

郭瑜1,2,3,陈超1,潘彦明2,汪强兵2,3,吴琛3,周科朝1

- 1. 中南大学 粉末冶金国家重点实验室, 长沙 410083;
- 2. 广州赛隆增材制造有限责任公司,广州 510700;
- 3. 西北有色金属研究院 金属多孔材料国家重点实验室, 西安 710016

摘 要:采用电子束粉末床熔融技术制备菱形十二面体、G7 及简单立方 3 种孔结构的多孔钽支架。通过压缩试验、拉伸试验、三点弯曲试验及有限元模拟,研究孔结构对多孔钽支架变形行为和力学性能的影响。在压缩试验中,G7 和简单立方结构的多孔钽支架以杆筋的屈服变形为主,而菱形十二面体支架以弯曲变形为主,导致菱形十二面体多孔钽支架的压缩强度较低。另一方面,菱形十二面体多孔钽支架具有较好的拉伸性能和弯曲性能。在拉伸变形和弯曲变形中,菱形十二面体多孔钽支架的最大应力分布均匀,均匀的结构变形使得杆筋断裂延缓;而G7 和简单立方结构多孔钽支架由于应力集中在横杆上,变形初期即出现杆筋断裂。因此,应根据不同的力学性能需求,合理选择电子束选区熔化多孔钽支架的孔结构。

关键词: 增材制造; 多孔钽支架; 电子束粉末床熔融; 孔结构; 变形行为; 力学性能

(Edited by Wei-ping CHEN)